

APPLIED SCIENCES AND ENGINEERING

Wireless battery-free wearable sweat sensor powered by human motion

Yu Song^{1,2*}, Jihong Min^{1*}, You Yu¹, Haobin Wang², Yiran Yang¹, Haixia Zhang², Wei Gao^{1†}

Wireless wearable sweat biosensors have gained huge traction due to their potential for noninvasive health monitoring. As high energy consumption is a crucial challenge in this field, efficient energy harvesting from human motion represents an attractive approach to sustainably power future wearables. Despite intensive research activities, most wearable energy harvesters suffer from complex fabrication procedures, poor robustness, and low power density, making them unsuitable for continuous biosensing. Here, we propose a highly robust, mass-producible, and battery-free wearable platform that efficiently extracts power from body motion through a flexible printed circuit board (FPCB)-based freestanding triboelectric nanogenerator (FTENG). The judiciously engineered FTENG displays a high power output of $\sim 416 \text{ mW m}^{-2}$. Through seamless system integration and efficient power management, we demonstrate a battery-free triboelectrically driven system that is able to power multiplexed sweat biosensors and wirelessly transmit data to the user interfaces through Bluetooth during on-body human trials.

Copyright © 2020
The Authors, some
rights reserved;
exclusive licensee
American Association
for the Advancement
of Science. No claim to
original U.S. Government
Works. Distributed
under a Creative
Commons Attribution
NonCommercial
License 4.0 (CC BY-NC).

INTRODUCTION

Prolific research toward the development of wearable bioelectronic technologies is greatly expanding the horizons of personalized health monitoring (1–4). Wireless wearable devices offer a noninvasive means of extracting real-time physiological parameters indicative of health status and transmitting continuous data to a user device. Wearable devices capable of detecting various vital signs such as pulse, respiration rate, and temperature are being widely commercialized and integrated into daily lifestyles (5–9). Sweat is another attractive medium containing a multitude of molecular biomarkers including electrolytes, metabolites, amino acids, hormones, and drugs that wearable sensors can analyze (10–15). Continuous monitoring of these biomarkers has the potential to supplement laboratory-based blood tests in enabling real-time monitoring of daily health status as well as early disease detection and management (15–20).

Over the past years, extensive interest and efforts have focused on developing novel sensors and improving the wearability of these platforms (14, 21). Until now, most wearable sensor prototypes relied on bulky and rigid battery packs to power the electronic circuitry for data acquisition, processing, and transmission. Flexible batteries have been proposed to enable conformal contact on skin (22, 23), and incorporation of low-power electronics has substantially reduced the power requirements of wearables and enabled the use of small coin cell batteries. Despite these efforts, batteries still face limitations in that they need to be charged and replaced frequently. In addition, while unlikely, lithium ion batteries are susceptible to explosion, posing safety concerns. Battery-free systems powered by near-field communication (NFC) are reported (24, 25) but could suffer from short operation distance. As an alternative, energy can be harvested from renewable, portable, and sustainable sources such as solar light, biofluids, and human motion to power future wireless wearable electronics (26–29).

Triboelectric nanogenerators (TENGs), which convert the mechanical energy created by human motion into electrical energy via coupling of inductive and triboelectric effects (30–35), offer a highly attractive energy harvesting strategy to power wearable sweat sensors during intensive physical activities as their operation is independent from uncontrollable external sources such as sunlight or wireless power transmitters. Despite the advantage, most of the existing TENG-based devices suffer from low power intensity, inefficient power management, and a lack of power continuity and longevity; thereby, the use of a TENG to continuously power a fully integrated wireless wearable molecular sensor system has not been reported (28, 36–39).

Here, we propose a battery-free, fully self-powered wearable system that consists of a highly efficient wearable freestanding-mode TENG (FTENG), low-power wireless sensor circuitry, and a microfluidic sweat sensor patch on a single flexible printed circuit board (FPCB) platform that can dynamically monitor key sweat biomarkers (e.g., pH and Na^+) (Fig. 1A). Such an FTENG-powered wearable sweat sensor system (FWS³) is designed and prepared to be compatible with traditional FPCB manufacturing processes, which enables mass productivity and high reliability. Our freestanding FPCB-based design, coupled with effective power management, allows efficient energy harvesting from human skin, particularly suitable for powering skin-interfaced wearables. With the aid of waterproof medical tape, the FWS³ can be conformally laminated on the side torso to maximize the potential for energy harvesting (Fig. 1, B and C). The integrated Bluetooth Low Energy (BLE) module allows sensor data to be conveniently transmitted to a mobile interface for health status tracking during exercise. This represents the first demonstration of a fully integrated battery-free triboelectrically driven wearable system for multiplexed sweat sensing.

RESULTS

Design of the FWS³

The FTENG consists of an interdigital stator and a grating-patterned slider (Fig. 1D). To obtain a strong electrification effect, polytetrafluoroethylene (PTFE) and copper are used as tribo-pairs in the

¹Andrew and Peggy Cherng Department of Medical Engineering, California Institute of Technology, Pasadena, CA 91125, USA. ²National Key Lab of Micro/Nano Fabrication Technology, Peking University, Beijing 100871, China.

*These authors contributed equally to this work.

†Corresponding author. Email: weigao@caltech.edu

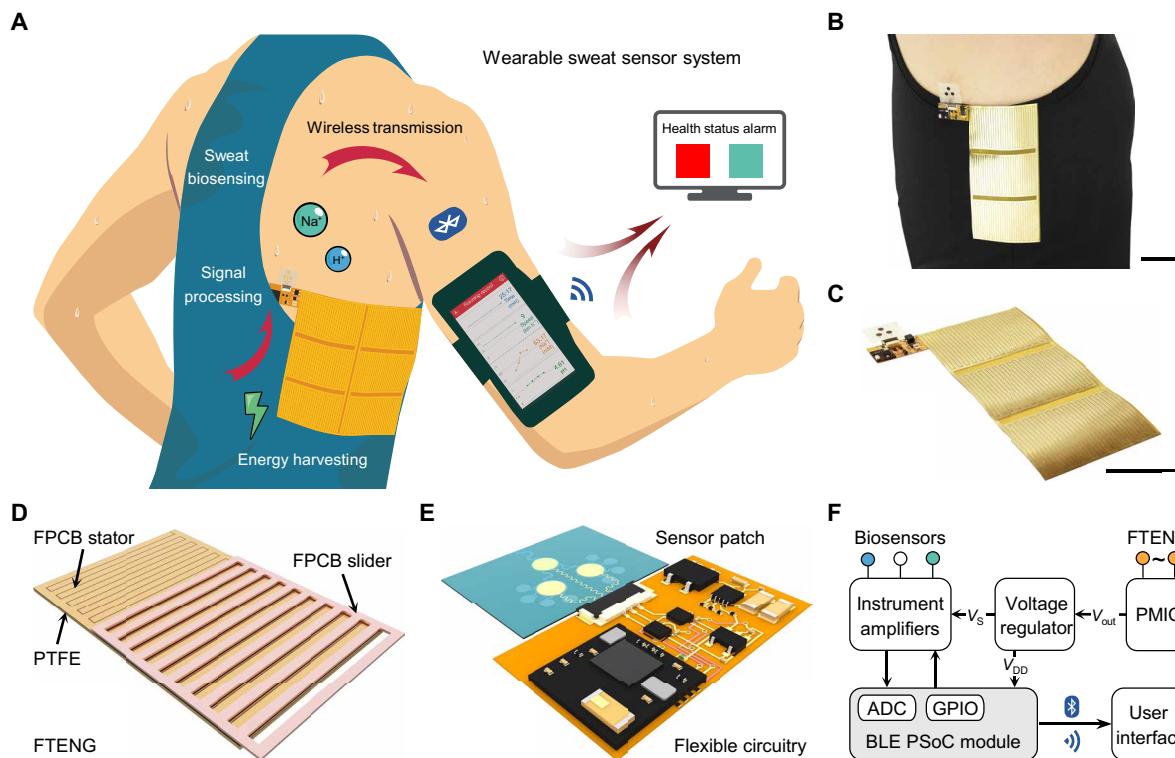


Fig. 1. Battery-free FWS³ for wireless and noninvasive molecular monitoring. (A) Schematic illustrating the FWS³ that integrates human motion energy harvesting, signal processing, microfluidic-based sweat biosensing, and Bluetooth-based wireless data transmission to a mobile user interface for real-time health status tracking. (B and C) Optical images of an FPCB-based FWS³, which can be worn on a human side torso. Scale bars, 4 cm. (D) Schematic diagram of the FPCB-based FTENG with a grating slider and an interdigital stator. (E) Schematic diagram of the FWS³ showing a microfluidic-based sweat sensor patch interfacing with the flexible circuitry. (F) System-level block diagram showing the power management, signal transduction, processing, and wireless transmission of the FWS³ from the FTENG to the biosensors, then to the user interface. Photo credit: Yu Song, California Institute of Technology.

flexible FTENG. The FTENG is fabricated through commercial FPCB technology (as illustrated in fig. S1), and the detailed dimensional parameters are shown in fig. S2. The inter-electrode distance was optimized through transferred charge density studies of the FTENGs (fig. S3). The stator and slider are patterned through photolithography as the periodically complimentary interdigital structure and the grating structure, respectively. With an electroless nickel/immersion gold (ENIG) surface finish on the electrode area, the stator is further laminated by PTFE. The reusable flexible circuitry in conjunction with a disposable microfluidic sweat sensor patch can continuously perform electrochemical measurements of key biomarkers in sweat (Fig. 1E). During exercise, the FTENG generated power is stored and released from a capacitor as controlled by the power management integrated circuit (PMIC) (Fig. 1F). When fully charged, the storage capacitor releases its stored energy, which is regulated to a stable voltage to power the BLE programmed system on a chip (PSoC) module and instrumentation amplifiers for acquisition and transmission of potentiometric measurements over BLE.

Characterization of the FTENG

The working mechanism of the FTENG can be explained as the coupling effect of contact electrification and in-plane sliding-induced charge transfer, as illustrated in Fig. 2A. As copper is more triboelectrically positive than PTFE, electrons accumulate on PTFE during the sliding process. In the initial state, the grating slider fully overlaps with one stator electrode and no charge flow occurs be-

tween the interdigital stator electrodes due to the electrostatic equilibrium. The unidirectional sliding process results in a charging flow between stator electrodes until the grating slider fully overlaps with the second stator electrode with reversed polarity. This working process was further validated by numerical simulation using COMSOL Multiphysics (fig. S4). The detailed model of the FTENG under open-circuit and short-circuit conditions is explained in fig. S5 and notes S1 and S2. The optical microscopic image of our proposed FPCB-based FTENG and the typical short-circuit current (I_{SC}) profiles of an FTENG at different working frequencies are shown in Fig. 2 (B and C). The FTENG operates consistently at varying frequencies of 0.5, 1.25, and 3.3 Hz, resulting in the maximum I_{SC} of 8.39, 19.11, and 42.25 μ A, respectively. The open-circuit voltage (V_{OC}) attained at the frequency of 0.5 Hz is presented in fig. S6A, where the signal polarity of the envelope waveform oscillates rapidly along the sliding process. To evaluate the use of our FPCB-based FTENG as a power source, the voltages and powers are measured under a series of different load resistances (Fig. 2D), with a working frequency of 1.5 Hz for actuation. An increase of resistance beyond 1 megohm leads to a rapid increase of voltage. With a load resistance of 4.7 megohms, the FTENG reaches a maximum power output of 0.94 mW (corresponding to 416 mW m⁻²).

The PTFE of the FPCB-based FTENG displays superior durability performance over conventional micro-pyramid polydimethylsiloxane (M-PDMS) and wrinkled PDMS (W-PDMS) after 20,000 working cycles (Fig. 2E), where the V_{OC} experiences minimal decay

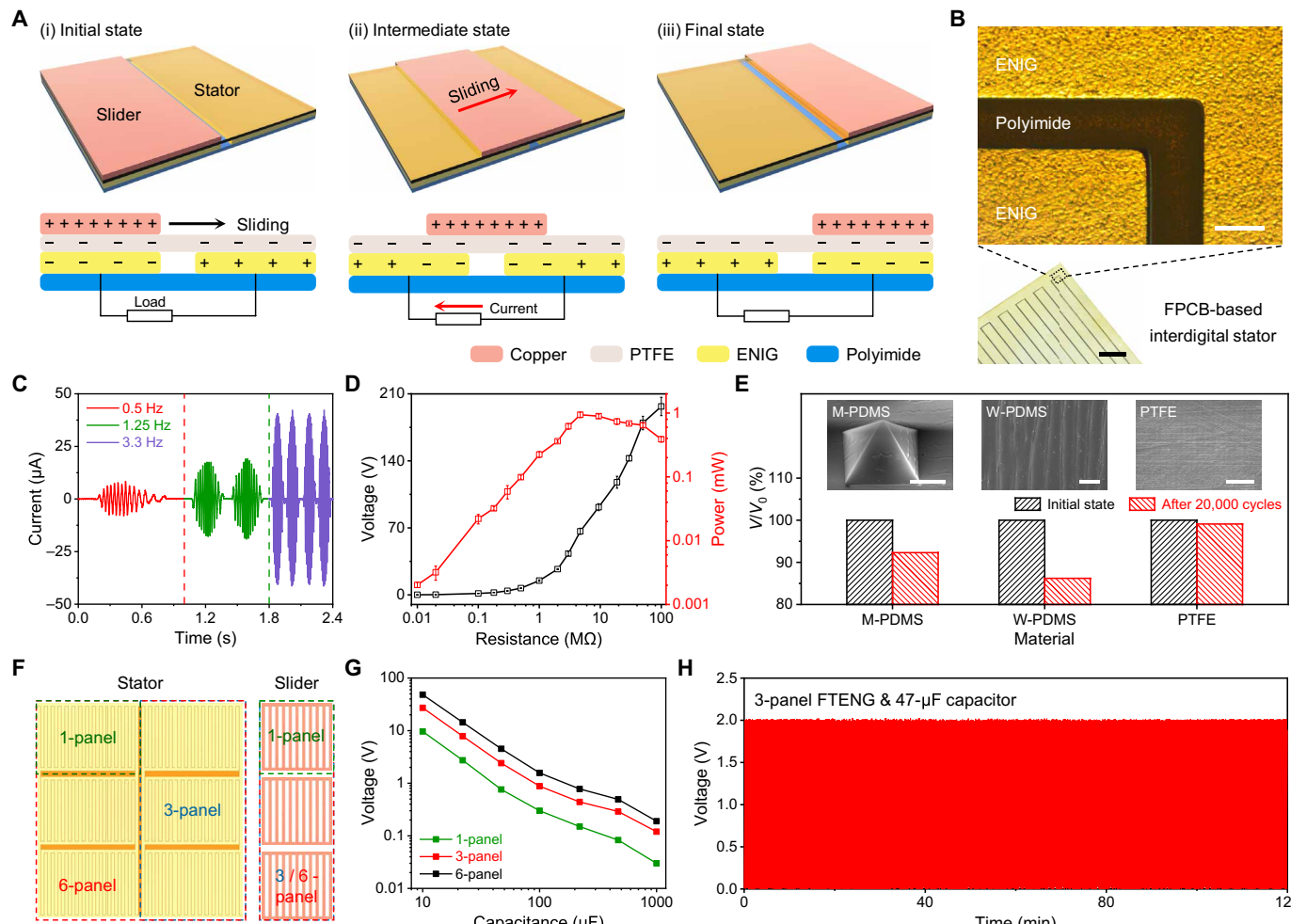


Fig. 2. Characterization of the FTENG for energy harvesting from human motion. (A) Schematic illustration of the working mechanism and charge distribution of the FTENG. (B) Microscopic and optical images of an FPCB-based interdigital stator with an ENIG surface finish on the patterned electrode area. Scale bars, 200 μ m and 5 mm. (C) Current output of an FTENG under different working frequencies. (D) Peak voltage and the corresponding average power of an FTENG at different external load resistances ($n = 5$). Working frequency, 1.5 Hz. (E) Durability of M-PDMS-, W-PDMS-, and PTFE-based stators after 20,000 test cycles. V and V_0 represent the peak open-circuit voltage after and before the durability test. Inset images, SEM images of M-PDMS, W-PDMS, and PTFE after 20,000 test cycles. Scale bars, 5, 50, and 50 μ m. (F) Schematic of the flexible FTENG with different stator layouts (one, three, or six panels in parallel) and corresponding slider layouts. (G) Comparison of voltages of the capacitors ranging from 10 to 1000 μ F charged with one-, three-, and six-panel FTENGs for 30 cycles. (H) Long-term stability of a three-panel FTENG in charging a 47- μ F capacitor under a working frequency of 1.5 Hz for 2 hours.

as displayed in fig. S6B. The scanning electron microscopy (SEM) images in Fig. 2E and fig. S7 reveal the morphologies of different triboelectric materials before and after the durability test: The PTFE shows great mechanical robustness without scratches, while both M-PDMS and W-PDMS suffer notable surface damage. The influence of normal force and shear force (reflected by sliding frequency) on the performance of the FTENG during regular use is demonstrated in fig. S8: The peak output voltage increases and then saturates with the increase of normal forces, while the output voltage remains stable under varied sliding frequencies for a given normal force. The FTENG is mechanically robust and shows similar electrical output even under a high normal force of 100 N. The FTENG's response is stable after 1000 bending cycles (radius of curvature, 5 cm) (fig. S9) and under varied physiological temperatures (fig. S10). Moreover, the FTENG could maintain high performance after 100 washing cycles, indicating superior wearable capabilities

over conventional TENGs (fig. S11 and table S1). In designing future TENG-powered devices, it is important to consider factors such as cost, materials, mechanical properties, and power density. TENGs commonly prepared through fabric weaving and polymer coating processes are very low cost but limited by low fabrication resolution and reproducibility. In contrast, the FPCB-based FTENG offers a high-resolution, cost-effective, and mechanically robust energy harvesting solution.

To meet the high energy demands of the wearable sensors, one, three, and six panels of the FTENGs, designed by taking consideration of the size of human side torso, were further evaluated by capacitor charging (Fig. 2F). The output of the FTENG was rectified with a full-wave rectifier. These different FTENG layouts were each actuated for 30 working cycles to charge capacitors ranging from 10 to 1000 μ F (Fig. 2G). For the capacitor with 1000 μ F, 0.03, 0.12, and 0.19 V could be obtained for one, three, and six panels, respectively,

showing great charging capability. At a working frequency of 3.3 Hz, the six-panel FTENG showed a maximum transferred charges (σ_{SC}) of 15.73 μ C during one working cycle (fig. S12A). Meanwhile, fig. S12B portrays the charging-discharging curves of different capacitors charged to 2 V with a three-panel FTENG at a working frequency of 2 Hz. The three-panel FTENG, actuated at a working frequency of 1.5 Hz, was able to repetitively charge a 47- μ F capacitor over a 2-hour duration from 0 to 2 V (Fig. 2H), indicating high long-term cycling stability. The FTENGs can also be used to charge capacitors of various capacitances at different cycle lengths (fig. S13). Depending on the application, connecting several FTENGs in parallel can be a practical and attractive strategy to greatly increase power output.

Design and characterization of microfluidic sweat sensor patch

Figure 3A depicts the schematic of the dual biosensor array used for sweat analyte analysis based on ion-selective electrodes (ISEs). Laser-engraved microfluidic channels are assembled onto the sensing patch. Detailed fabrication procedures are listed in Materials and Methods and fig. S14. The Ag/AgCl reference electrode is coated with polyvinyl butyral (PVB) to sustain a steady potential for the potentiometric measurements of various electrolytes in sweat regardless of solution ionic strength. For pH analysis, the deprotonation of H^+ atoms on the surface of the electrodeposited polyaniline (PANI) layer is measured as an indicator of bulk H^+ concentration. Na^+ concentration measurements are facilitated by a thin ion-selective membrane containing a Na^+ ionophore X and a poly(3,4-ethylenedioxythiophene (PEDOT):poly(sodium 4-styrenesulfonate) (PSS) layer in between the gold electrode layer and sodium ion-selective membrane as an ion-electron transducer that can minimize the potential drift of the biosensor. As depicted in Fig. 3 (B and C), the pH and Na^+ sensors display near-Nernstian sensitivities of 56.28 and 58.63 mV per decade concentration, respectively, in physiologically relevant pH levels (4 to 8) and Na^+ concentrations (12.5 to 200 mM). Both sensors show excellent selectivity, reproducibility, and long-term stability (figs. S15 to S17), and their responses remain stable under different physiological temperatures (fig. S18), making them suitable for wearable continuous monitoring.

Laser patterned microfluidic layers were attached onto a polyethylene terephthalate (PET) sensor substrate in a sandwich structure (medical-tape/PDMS/medical-tape) for controlled and automated on-body sweat sampling (Fig. 3D and fig. S19). To validate the performance of the microfluidic system, dynamic biosensing was performed during continuous flow injection of Na^+ solutions at varying physiologically relevant sweat rates (1, 2, and 4 μ l min⁻¹) (Fig. 3E). When the Na^+ concentration was switched from 50 to 200 mM at a flow rate of 2 μ l min⁻¹, the Na^+ sensor took ~2 min to reach new stable readings. The high temporal resolution is repeatable over multiple concentration change cycles (Fig. 3F). The flexible microfluidic sensor patch can conformally adhere to human skin (Fig. 3G) and shows excellent mechanical stability through rigorous bending tests (radius of curvature, 2 cm), indicating their potential for wearable applications in various physical activities (Fig. 3, H and I).

System-level integration for energy management and low-power biosensing

As aforementioned, the FWS³ consists of an interdigital FENG stator, a PMIC, a low-dropout voltage regulator, two low-power

instrumentation amplifiers, and a BLE PSoC module seamlessly integrated onto a polyimide-based PCB. In addition, the full platform requires a grating-patterned FTENG slider and a microfluidic sensor patch. For design compatibility and flexibility, the FTENG and electronic circuitry were designed on a single PCB design software. The detailed part list and circuit diagram for the flexible circuitry are shown in figs. S20 and S21, respectively. A block diagram illustrating the electrical connections between the modules is shown in Fig. 4A. For optimal power management, a commercial energy harvesting PMIC was adopted to manage power generated by the FTENG with minimal power waste. With the aid of a bridge rectifier that converts the high voltage AC signal generated by the FTENG into a DC signal, the PMIC stores the FTENG generated power in two capacitors in parallel (220 and 22 μ F). The three SET_V_{OUT} resistors set the programmable threshold and hysteresis voltages such that the stored power is released only when absolutely necessary through built-in switch control logic. When the voltage of the storage capacitors (V_{STORE}) reaches 3.5 V, the capacitors supply energy to the load/output (V_{OUT}) until V_{STORE} decreases to 2.2 V. At 2.2 V, the PMIC's control unit disconnects the storage capacitors from the load/output until the storage capacitors are charged back to 3.5 V. When supplied by the storage capacitors, the load/output voltage is regulated to 2.2 V by a voltage regulator to provide a stable voltage for the precise measurement circuitry.

Efficient power management is matched with low-power measurement via low-power instrumentation amplifiers with shutdown modes, and low-power data transmission via connectionless BLE advertisements to enable FTENG-powered wearable and wireless sweat analysis. Every time the storage capacitor is charged to 3.5 V, the BLE PSoC module initiates one ~510-ms operation cycle as portrayed in the flow diagram (Fig. 4B). After startup of the main processor, the PSoC pulls a general-purpose input/output (GPIO) pin high to wake up the two instrumentation amplifiers from shutdown. After initialization of the instrumentation amplifiers, the PSoC's embedded 12-bit ADC (analog-to-digital converter) samples and averages 32 potentiometric measurements acquired through the instrumentation amplifiers. After ADC measurements, the instrumentation amplifiers are shut down to minimize power consumption. The BLE submodule of the PSoC requires the 32-kHz watch crystal oscillator (WCO) for accurate operation, which has a maximum startup time specification of 500 ms. Therefore, after the ADC measurements, the main processor of the PSoC starts the WCO and goes into deep sleep for 500 ms where it consumes ~2 μ A. Then, the BLE stack initializes and the ADC measurements are advertised to a nearby BLE observer user device. The detailed power consumption breakdown of the circuit including the voltage regulator, BLE PSoC module, and two instrumentation amplifiers is shown in Fig. 4C. When supplied with 2.2 V, the circuit consumes an average of 330 μ A during ~510 ms (168 μ C).

Several studies were performed to validate the robust operation of the fully integrated system. The three-panel FTENGs were activated via sliding motion at frequencies ranging from 2 to 1 Hz to simulate human arm swing during exercise (40). The resultant charging and discharging cycles of the storage capacitors are shown in Fig. 4D. Furthermore, to validate the operation of the low-power wireless sensor circuitry, the potentiometric inputs were simulated by using a DC power supply to apply voltages ranging from 100 to 300 mV (charged every 300 s) across the reference and working electrode pins (Fig. 4E). These simulated sensor inputs were accurately

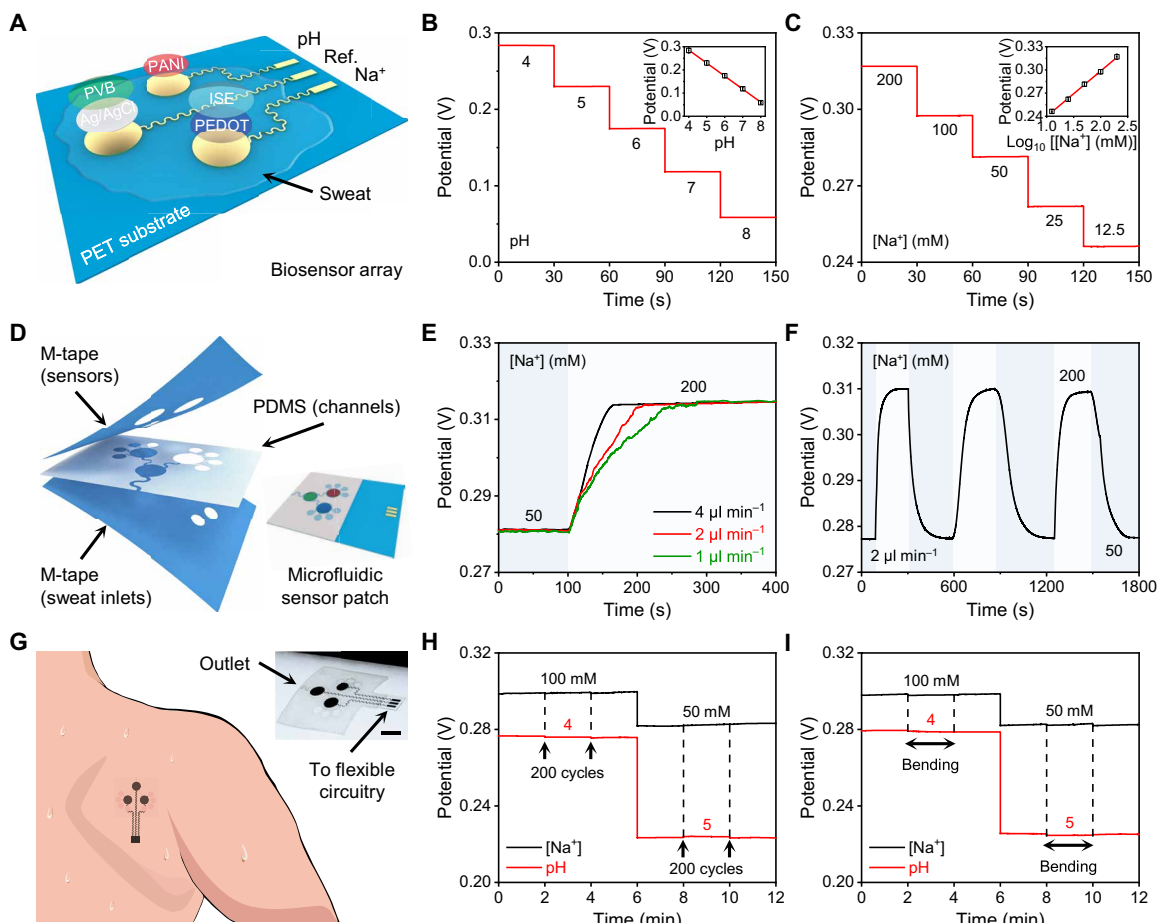


Fig. 3. Characterization of the microfluidic-based biosensor patch in vitro. (A) Schematic of a flexible biosensor array containing a pH sensor and a Na⁺ sensor patterned on a flexible PET substrate. (B and C) Open-circuit potential responses of a pH sensor in standard McIlvaine's buffer solutions (B) and a Na⁺ sensor in NaCl solutions (C). Insets show the corresponding calibration plots of each sensor. Error bars represent the SDs from six independent tests. (D) Schematic of the microfluidic design for dynamic sweat sampling. M-tape, medical tape. (E) Dynamic response of a Na⁺ sensor under different flow rates upon switching the solution concentrations. (F) Repeatability of dynamic response of a Na⁺ sensor by continuously switching the inflow solutions at a flow rate of 2 $\mu\text{l min}^{-1}$. (G) Schematic of microfluidic sensor patch conformally attached to human skin. Inset image, optical image of a microfluidic sensor patch under mechanical deformation. Scale bar, 5 mm. (H and I) Responses of a Na⁺ and pH sensor array after 0, 200, and 400 cycles of bending (H) and during bending states (I) (radius of curvature, 2 cm). Data recording was paused for 30 s to change the conditions and settings. Photo credit: Yu Song, California Institute of Technology.

measured and transmitted by the FPCB platform while being powered by a three-panel FTENG actuated at various working frequencies. The long-term stability of the whole FWS³ system is demonstrated by using the FTENG to power the FPCB for more than 4 hours, during which pH and Na⁺ concentrations in collected human sweat were measured for an hour (Fig. 4, F and G). Furthermore, the long-term durability of the FPCB-based FTENG was tested by comparing its ability to power the whole platform after 1 month of its initial use (fig. S22). Improvements in wireless data transmission in terms of transmission interval can be attained by further advancing the power density and efficiency of the FTENG.

On-body evaluation of the FWS³ in prolonged physical activities

Common cardiovascular exercises such as running, rowing, and elliptical training induce a sliding motion between the side of the torso and the inner arm. Taking advantage of this mechanical motion, the stator of FTENG can be fixed on the side torso, and the

slider of FTENG can be attached to the inner part of the arm. For on-body evaluation, a six-panel stator FTENG-based FWS³ was used for increased power output (as illustrated in fig. S23). The FTENG power output waveforms during various exercises are shown in Fig. 5A. Treadmill running was chosen as the exercise to perform on-body validation experiments for the entire system. The FPCB's storage capacitor charging and discharging curve during a 60-min constant speed running session shows that up to 18 operation cycles can be achieved (Fig. 5B). The length of charging/discharging cycle ranges from 2.1 to 3.7 min (Fig. 5C). It should be noted that the system generates power when the stator and slider physically rub against each other; the charge in the capacitor will accumulate without discharge whenever there is rubbing motion; when the capacitor is charged to a threshold voltage, the capacitor will discharge and power a single measurement event. Despite duration variations in capacitor charging/discharging cycles caused by varied rubbing area, forces, and frequencies, the FWS³ system proved itself to be fully functional during normal physical exercises (fig. S24).

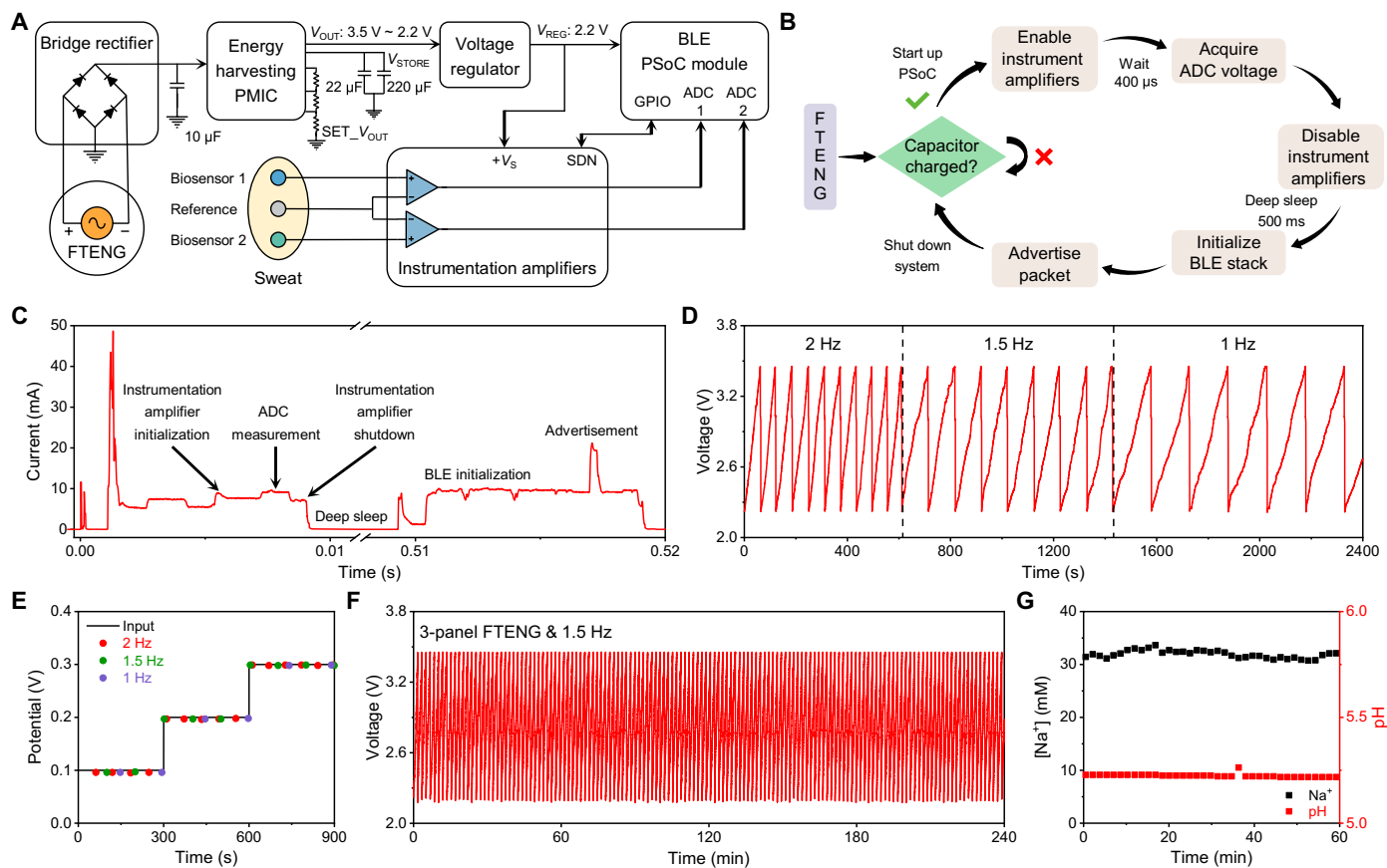


Fig. 4. System-level integration and evaluation of the FWS³. (A) Schematic diagram of the battery-free FWS³ consisting of an FTENG module, a biosensor interface, instrumentation amplifiers, an energy harvesting PMIC, a voltage regulator, and a BLE PSoC module. (B) Operation flow of the FWS³ with signal processing and data transmission. (C) Power consumption of the FWS³ during the operation. (D) Real-time potential of the capacitor (242 µF) during the continuous operation of the FWS³ with a three-panel FTENG under different working frequencies. (E) Validation of data transmission from an FWS³ with a three-panel FTENG under different working frequencies. (F) Long-term stability of the capacitor charging process when an FWS³ operates under a working frequency of 1.5 Hz. (G) Sensor responses in a collected human sweat sample when an FWS³ operates under a working frequency of 1.5 Hz.

On-body performance of the entire FWS³ was evaluated on a healthy subject through treadmill running at a constant speed of 9 km hour⁻¹. Two wearable systems, charged by the FTENG and the battery, were placed on the back of the subject. The physiological information collected by both systems were wireless-transmitted to a user interface through BLE for further analysis (Fig. 5D). Five measurements were recorded from the FWS³ during the 30-min exercise; stable pH levels and increased Na⁺ levels were observed from both systems (Fig. 5E), confirming the accuracy of the battery-free FWS³ for on-body sensing. The noise contribution during various exercises performed by the subjects wearing an FWS³ is insignificant in comparison to the sensor signal of interest (fig. S25). These data demonstrate the potential of the self-powered wearable platform for continuous monitoring of various physiological biomarkers in sweat during exercise.

DISCUSSION

The emerging wearable technologies have enabled numerous personalized medical applications. Wearable sweat analysis has the potential to achieve noninvasive and continuous monitoring of an individual's health status at molecular levels. Owing to the multi-

functioning and multitasking requirements, wearable sweat biosensors usually have high power consumption. Batteries are the primary power source of most of the wireless e-skin systems but usually suffer from limited usability, especially when there is limited electricity availability. Given that a major application of sweat sensing is health and fitness tracking during vigorous exercise, energy harvesting from the human body is a promising approach for powering future wearable sweat sensors, particularly the ones that can convert biomechanical energies from human motion into electricity.

The advent of TENG technology sparked great excitement due to its potential application in self-powered systems, particularly for wearable and implantable electronics. As a newly emerging technique for energy conversion, TENGs face major challenges that need to be addressed for practical applications. First, TENG signals are essentially high-voltage pulses and insufficient to meet real-time energy consumption for wearable electronics; second, for wearable continuous use, the longevity of TENGs needs to be improved due to the stability limitations of organic polymeric materials used for device fabrication. Last but not least, system integration of TENGs in wearable devices and demonstrations of their usability in practical applications are significantly underdeveloped.

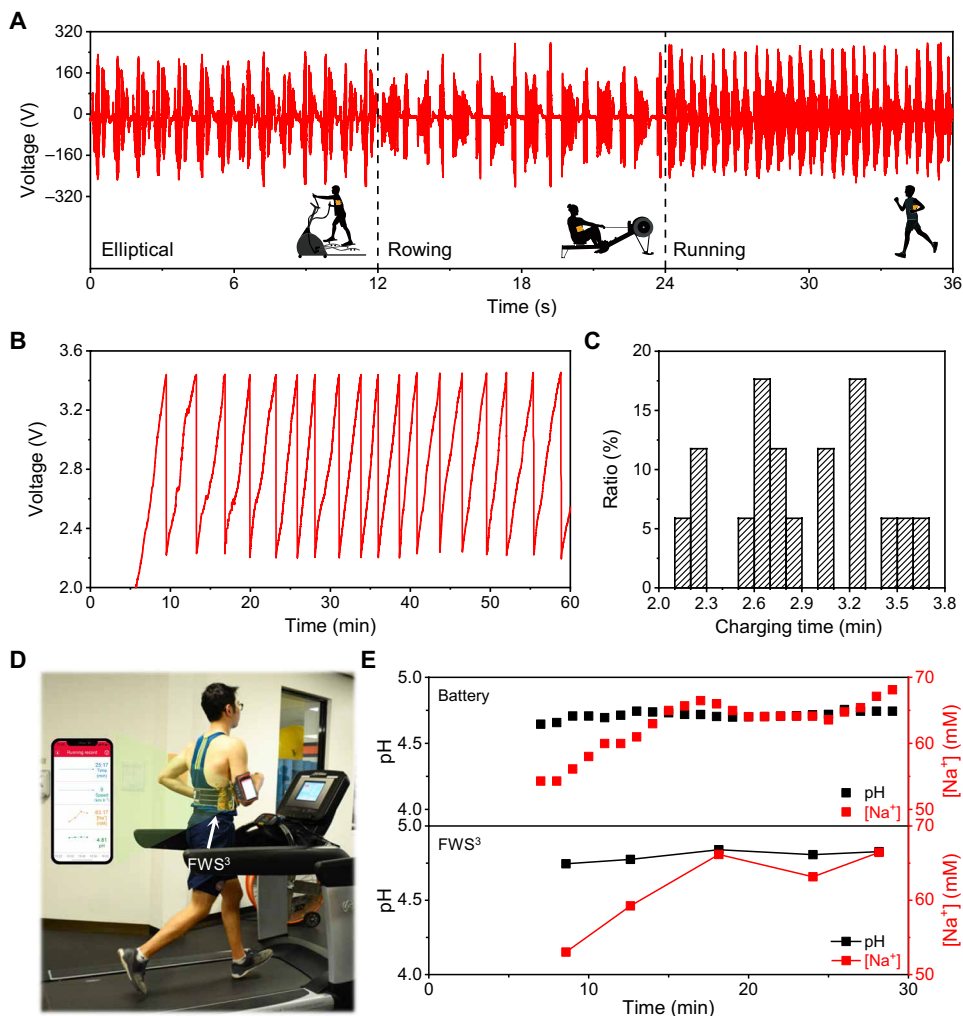


Fig. 5. On-body evaluation of the FWS³ for wireless, dynamic perspiration analysis. (A) Output waveforms of a six-panel FPCB-based FTENG during various exercises. (B and C) Real-time potential of the capacitor charged by an FTENG (B) and the average charging time for each package transmission (C) when a subject is running on a treadmill for 1 hour at a constant speed of 9 km hour⁻¹. The ratio in (C) represents the percentage of charging cycles (with charging duration within a given time range) out of all the charging cycles. When the potential reaches 3.3 V, the capacitor is discharged due to the BLE data transmission. (D) Optical image of a subject on a treadmill wearing an FWS³ and a mobile phone. (E) Real-time sweat pH and Na⁺ levels wirelessly obtained from the wearable systems charged by a lithium battery and by an FTENG during constant speed running. Photo credit: Yu Song, California Institute of Technology.

Here, we addressed these challenges by proposing a highly robust, mass-producible, fully self-powered battery-free wearable system that can efficiently and reliably harvest energy from human motion during vigorous exercises through an FPCB-enabled FTENG. As compared to traditional TENGs, the fabricated FTENG using commercial FPCB fabrication procedures shows remarkable mechanical and electrical stability even after intensive mechanical deformations and repeated washing cycles. Through seamless system integration and efficient power management, this fully flexible system is able to power multiplexed sweat biosensors and wirelessly send data to the user interfaces through Bluetooth during on-body human trials. Compared to previously reported TENG-based wireless sensor systems (table S2) that either are not wearable or require ultralong charging periods to perform measurements, the FWS³ represents a breakthrough in terms of practicality for wearable applications. We envision that, with further development, this technology could serve as a highly attractive approach toward self-powered wireless

personalized health monitoring during people's daily activities; it will also find numerous applications in environmental and defense areas.

MATERIALS AND METHODS

Materials

EDOT, PSS, sodium ionophore X, bis(2-ethylhexyl) sebacate (DOS), PVB, polyvinyl chloride (PVC), sodium tetrakis[3,5-bis(trifluoromethyl)phenyl] borate (Na-TFPB), aniline, sodium thiosulfate pentahydrate (Na₂S₂O₃), sodium bisulfite (NaHSO₃), calcium chloride dihydrate (CaCl₂·2H₂O), block polymer PEO-PPO-PEO (F127), multiwall carbon nanotubes (MWCNTs), iron(III) chloride (FeCl₃), potassium hydroxide (KOH), and citric acid were purchased from Sigma-Aldrich. Sodium chloride (NaCl), ammonium chloride (NH₄Cl), methanol, ethanol, acetone, tetrahydrofuran (THF), hydrochloric acid (HCl), tetrachloroauric acid (HAuCl₄), and disodium phosphate (Na₂HPO₄) were purchased from Thermo Fisher Scientific. PDMS

(SYLGARD 184) was purchased from Dow Corning. Silver nitrate (AgNO_3) was purchased from Alfa Aesar. Waterproof, double-sided medical tapes (75 μm thick) were purchased from Adhesives Research. Silver conductive paint was purchased from Structure Probe Inc. (SPI) supplies. Moisture-resistant PET film (100 μm thick) was purchased from McMaster-Carr. PTFE (50 μm thick) was purchased from JIAET.

Design and fabrication of the FPCB module

The FPCB module for the FTENG and electronic circuit was designed using Eagle CAD (Autodesk). The BLE PSoC module was programmed in the PSoC Creator Integrated Design Environment (Cypress Semiconductor). A full list of components for the circuit design provided in fig. S20 includes power management units (MB10S-13, Diodes Incorporated; S6AE101A, Cypress Semiconductor; TPS7A05, Texas Instruments), a BLE PSoC module (CYBLE-022001-00, Cypress Semiconductor), potentiometric sensing units (AD8235, Analog Devices), and passive components. A detailed circuit diagram is shown in fig. S21.

The flexible circuitry and FTENG were fabricated by a commercial FPCB manufacturer (detailed fabrication process shown in fig. S1). Two sheets of commercial flexible copper clad laminates (120 μm thick; JingHuang Electronics Co.), consisting of a flexible polyimide substrate and a copper film, sandwich a thin layer of epoxy adhesive. The copper films were patterned by photolithography and etched by a FeCl_3 solution to fabricate the circuit elements and interdigital electrode of the stator, and complementary grating structures of the slider. An ENIG layer was deposited to protect the stator electrode. Last, a layer of PTFE was laminated on the interdigital electrode of the stator to induce electrification. The total size of one-panel stator of the FTENG is 22.6 cm^2 (length, 5.78 cm; width, 3.78 cm). The weight of one-panel stator of the FTENG is 0.586 (without PTFE coated) and 0.782 g (with PTFE coated). The total size and weight of one-panel slider of the FTENG are 18.22 cm^2 (length, 4.36 cm; width, 4.18 cm) and 0.396 g, respectively.

Characterization of the FTENG

For the output performance of the FTENG, a digital oscilloscope (Agilent DSO-X 2014A) was adopted to test the open-circuit voltage with a 100-megohm probe. The short-circuit current was amplified by an SR570 low-noise current amplifier from Stanford Research Systems. The COMSOL software was used to simulate and verify the electrostatic stimulation during the sliding process.

PDMS with microstructures (M-PDMS and W-PDMS) were involved in durability test as the triboelectric materials under the contact-separation mode. The elastomer and cross-linker of PDMS were mixed first, with a quantity ratio of 10:1. For the M-PDMS, the vacuum-degassed solution was spin-coated on the Si wafer with inverted pyramid structure (fabricated by photolithography and KOH wet etching). When the PDMS was partially cured, one piece of FPCB-based stator ($3 \times 4 \text{ cm}^2$) with ENIG electrode was coated among it. After cured at 80°C for 2 hours, the stator was peeled off with prepared M-PDMS. For the W-PDMS, the cured PDMS was prestretched with the strain of 30% and carried out with ultraviolet ozone treatment by commercial ultraviolet lamp (Hangzhou Yaguang Lighting). After releasing process, the W-PDMS is conducted and coated on another FPCB-based stator. During the durability test, the maximum gap between PDMS and another triboelectric material (copper) is fixed at 3 mm at the working frequency of 2 Hz.

For the washing test, the FPCB-based FTENG was first rinsed with deionized (DI) water (25°C) and bath-sonicated for 10 min. Then, FTENG was fully dried at 60°C with 10 min for later measurement.

For the long-term stability study of the FTENG (fig. S22), the test was performed under the same conditions before and after a 1-month period. During the 1-month hiatus, the FTENG was stored in a plastic box in a regular office drawer at room temperature.

The morphology microscopic image of interdigital stator electrode was characterized by an optical microscope (Carl Zeiss AXIO). SEM images of the PTFE, M-PDMS, and W-PDMS were acquired with a field emission environmental SEM (FEI Quanta 600F).

Fabrication of microfluidic sensor patch

The fabrication of the electrode array is demonstrated in fig. S14. After pretreatment of the PET substrate, E-beam evaporation was used to deposit 20 nm of Cr and then 100 nm of Au onto a PET substrate to form the 3-mm-diameter gold electrodes. The electrode arrays were additionally coated with 1 μm of Parylene C (ParaTech LabTop 3000 Parylene coater) and patterned through photolithography. The fabricated array was further etched with O₂ plasma via reactive ion etching (Oxford III-V System 100 ICP/RIE) to remove the parylene layer at the designated sensing area. Then, the electrodes were modified and deposited with different functional materials to form the Na⁺ and pH working electrodes with a shared Ag/AgCl reference electrode. A CO₂ laser cutter was used to pattern the microfluidic layers. A waterproof double-sided medical tape layer patterned with 3-mm-diameter chambers was first attached to the PET sensor substrate. Then, a PDMS layer (100 μm thick) patterned with 3-mm-diameter reservoirs, inlets, an outlet, and fluidic connections was adhered onto the medical tape. Last, another medical tape layer patterned with inlets was attached on the PDMS layer.

Preparation of biosensors

An electrochemical workstation (CHI 860, CH Instruments) was used for electrochemical deposition and sensor characterization. For the Ag/AgCl reference electrode, an Ag deposition solution (0.25 M AgNO_3 , 0.75 M $\text{Na}_2\text{S}_2\text{O}_3$, and 0.43 M NaHSO_3) was used to deposit Ag on the Au electrode through constant voltage electrodeposition (-0.25 V for 600 s). Next, 0.1 M FeCl_3 was drop-casted onto the Ag for 30 s to form Ag/AgCl. A total of 6.6 μl of the PVB reference cocktail (79.1 mg of PVB, 50 mg of NaCl, 1 mg of F127, and 0.2 mg of MWCNT in 1 ml of methanol) was drop-casted on the Ag/AgCl electrode and left overnight to dry. The pH ISE was first modified by depositing Au (50 mM HAuCl₄ and 50 mM HCl) at 0 V for 30 s, followed by electropolymerizing PANI on the Au electrode in a bath (0.1 M aniline and 0.1 M HCl) through 50 cycles of cyclic voltammetry (-0.2 to 1 V at a scan rate of 50 mV s⁻¹). For the Na⁺ ISE, constant current electrodeposition (14 μA for 740 s) in a solution containing 0.01 M EDOT and 0.1 M NaPSS was used to deposit PEDOT:PSS on one Au electrode. Then, 15 μl of Na⁺ selective membrane cocktail was drop-coated onto the PEDOT:PSS layer and dried overnight. To prepare the cocktail, 100 mg of a mixture containing Na ionophore X (1%, w/w), Na-TFPB (0.55%, w/w), PVC (33%, w/w), and DOS (65.45%, w/w) was dissolved in 660 μl of THF.

Characterization of biosensor performance

To obtain the best performance for long-term continuous measurements, the biosensors were covered with a solution containing

0.1 M NaCl for 1 hour before measurements, which minimized the potential drift. For in vitro characterization, NaCl solutions with concentrations of 12.5, 25, 50, 100, and 200 mM in DI water, and McIlvaine's buffers with pH values ranging from 4 to 8 were used unless stated otherwise. Considering that there is variation in the absolute potential values for ion-selective sensors in the same solution, one-point calibration in a standard solution is essential. Here, a 25 mM NaCl solution was used to calibrate the biosensors before use for all tests.

Batches of biosensors were characterized to verify their repeatability and reproducibility by varying the solutions. Interference studies were performed by the successive addition of chloride solutions containing 50 mM NH₄⁺, 50 mM K⁺, and 50 mM Ca²⁺. All measurements were paused for 30 s while changing the solution. The long-term stabilities of pH and Na⁺ sensors were first tested continuously for 3 hours in a 100 mM NaCl solution and then evaluated for more than 6 weeks to check the sensitivity variation.

Previous work infers that pH in sweat remains relatively stable during exercise. Thus, the sampling capability of the microfluidic sensor patch is focused on the dynamic tracing of Na⁺. A syringe pump was used to inject solutions of different Na⁺ concentrations (50 and 200 mM) through the inlet of the microfluidic channels at varying flow rates. The mechanical reliability of the sensing patches was evaluated by bending them repeatedly on a three-dimensional-printed mold (radius of curvature, 2 cm) for 800 cycles. Sensor measurements were acquired every 200 cycles. In another study, continuous sensor measurements were recorded during active deformation of the sensors.

For the long-term sensor stability test (fig. S17), the biosensor arrays were tested every week under the same condition. Before weekly measurements, the sensor arrays were covered with a 0.1 M NaCl solution for 1 hour to minimize the potential drift. During the 6-week period, the ion-selective sensors were stored at ambient conditions under room temperature (25°C).

On-body evaluation of the FWS³

The validation and evaluation of the FWS³ were performed with human subjects at the gymnasium in compliance with all the ethical regulations under a protocol (ID 19-0892) that was approved by the Institutional Review Board at the California Institute of Technology. The participating healthy subjects, ages 20 to 35, were recruited from the California Institute of Technology. All subjects gave written, informed consent before participating in the study.

Subjects performed cardiovascular exercises using a running machine (Aeon), an elliptical machine (Precor), and a rowing machine (Stamina). Before exercise, the subject's upper back was wiped and cleaned with alcohol swabs and gauzes. Then, waterproof double-sided medical tape was used to adhere the FWS³ onto the subjects. The system including the FTENG stator was adhered to the side torso, and the FTENG slider was fixed onto the inner arm. To ensure accurate data, a new microfluidic sensor patch was used for each human trial. To evaluate the power output of the FTENG during the exercise, the output of the FTENG or the voltage across the storage capacitor was connected to an oscilloscope. When evaluating the entire system including the microfluidic sensor patch, the subjects were asked to run on a treadmill at a constant speed of 9 km hour⁻¹ for 30 min (to obtain sensor data regularly every several minutes); the BLE data were retrieved from a mobile phone or a personal computer. In addition, sweat samples were collected peri-

odically from the forehead of the subjects and pipetted into centrifuge tubes to be centrifuged at 6000 rpm for 15 min. The sweat samples were then frozen at -20°C for further testing.

SUPPLEMENTARY MATERIALS

Supplementary material for this article is available at <http://advances.sciencemag.org/cgi/content/full/6/40/eaay9842/DC1>

[View/request a protocol for this paper from Bio-protocol.](#)

REFERENCES AND NOTES

1. J. Kim, A. S. Campbell, B. E.-F. de Ávila, J. Wang, Wearable biosensors for healthcare monitoring. *Nat. Biotechnol.* **37**, 389–406 (2019).
2. T. R. Ray, J. Choi, A. J. Bandodkar, S. Krishnan, P. Gurutri, L. Tian, R. Ghaffari, J. A. Rogers, Bio-integrated wearable systems: A comprehensive review. *Chem. Rev.* **119**, 5461–5533 (2019).
3. T. Someya, Z. Bao, G. G. Malliaras, The rise of plastic bioelectronics. *Nature* **540**, 379–385 (2016).
4. Y. Yang, W. Gao, Wearable and flexible electronics for continuous molecular monitoring. *Chem. Soc. Rev.* **48**, 1465–1491 (2019).
5. D.-H. Kim, N. Lu, R. Ma, Y.-S. Kim, R.-H. Kim, S. Wang, J. Wu, S. M. Won, H. Tao, A. Islam, K. J. Yu, T.-i. Kim, R. Chowdhury, M. Ying, L. Xu, M. Li, H.-J. Chung, H. Keum, M. M. Cormick, P. Liu, Y.-W. Zhang, F. G. Omenetto, Y. Huang, T. Coleman, J. A. Rogers, Epidermal electronics. *Science* **333**, 838–843 (2011).
6. D. Son, J. Kang, O. Vardoulis, Y. Kim, N. Matsuhisa, J. Y. Oh, J. W. F. To, J. Mun, T. Katsumata, Y. Liu, A. F. McGuire, M. Krason, F. Molina-Lopez, J. Ham, U. Kraft, Y. Lee, Y. Yun, J. B.-H. Tok, Z. Bao, An integrated self-healable electronic skin system fabricated via dynamic reconstruction of a nanostructured conducting network. *Nat. Nanotechnol.* **13**, 1057–1065 (2018).
7. Q. Hua, J. Sun, H. Liu, R. Bao, R. Yu, J. Zhai, C. Pan, Z. L. Wang, Skin-inspired highly stretchable and conformable matrix networks for multifunctional sensing. *Nat. Commun.* **9**, 244 (2018).
8. C. Wang, X. Li, H. Hu, L. Zhang, Z. Huang, M. Lin, Z. Zhang, Z. Yin, B. Huang, H. Gong, S. Bhaskaran, Y. Gu, M. Makihata, Y. Guo, Y. Lei, Y. Chen, C. Wang, Y. Li, T. Zhang, Z. Chen, A. P. Pisano, L. Zhang, Q. Zhou, S. Xu, Monitoring of the central blood pressure waveform via a conformal ultrasonic device. *Nat. Biomed. Eng.* **2**, 687–695 (2018).
9. H.-R. Lim, H. S. Kim, R. Qazi, Y.-T. Kwon, J.-W. Jeong, W.-H. Yeo, Advanced soft materials, sensor integrations, and applications of wearable flexible hybrid electronics in healthcare, energy, and environment. *Adv. Mater.* **32**, 1901924 (2020).
10. W. Gao, S. Emaminejad, H. Y. Y. Nyein, S. Challa, K. Chen, A. Peck, H. M. Fahad, H. Ota, H. Shiraki, D. Kiriya, D.-H. Lien, G. A. Brooks, R. W. Davis, A. Javey, Fully integrated wearable sensor arrays for multiplexed *in situ* perspiration analysis. *Nature* **529**, 509–514 (2016).
11. H. Lee, T. K. Choi, Y. B. Lee, H. R. Cho, R. Ghaffari, L. Wang, H. J. Choi, T. D. Chung, N. Lu, T. Hyeon, S. H. Choi, D.-H. Kim, A graphene-based electrochemical device with thermoresponsive microneedles for diabetes monitoring and therapy. *Nat. Nanotechnol.* **11**, 566–572 (2016).
12. A. Koh, D. Kang, Y. Xue, S. Lee, R. M. Pielaik, J. Kim, T. Hwang, S. Min, A. Banks, P. Bastien, M. C. Manco, L. Wang, K. R. Ammann, K.-I. Jang, P. Won, S. Han, R. Ghaffari, U. Paik, M. J. Slepian, G. Balooch, Y. Huang, J. A. Rogers, A soft, wearable microfluidic device for the capture, storage, and colorimetric sensing of sweat. *Sci. Transl. Med.* **8**, 366ra165 (2016).
13. Y. Yang, Y. Song, X. Bo, J. Min, O. S. Pak, L. Zhu, M. Wang, J. Tu, A. Kogan, H. Zhang, T. K. Hsiao, Z. Li, W. Gao, A laser-engraved wearable sensor for sensitive detection of uric acid and tyrosine in sweat. *Nat. Biotechnol.* **38**, 217–224 (2020).
14. M. Bariya, H. Y. Y. Nyein, A. Javey, Wearable sweat sensors. *Nat. Electron.* **1**, 160–171 (2018).
15. R. M. Torrente-Rodríguez, J. Tu, Y. Yang, J. Min, M. Wang, Y. Song, Y. Yu, C. Xu, C. Ye, W. W. IsHak, W. Gao, Investigation of cortisol dynamics in human sweat using a graphene-based wireless mHealth system. *Mater. Matter* **2**, 921–937 (2020).
16. H. Lee, C. Song, Y. S. Hong, M. S. Kim, H. R. Cho, T. Kang, K. Shin, S. H. Choi, T. Hyeon, D.-H. Kim, Wearable/disposable sweat-based glucose monitoring device with multistage transdermal drug delivery module. *Sci. Adv.* **3**, e1601314 (2017).
17. J. Choi, R. Ghaffari, L. B. Baker, J. A. Rogers, Skin-interfaced systems for sweat collection and analytics. *Sci. Adv.* **4**, eaar3921 (2018).
18. S. Emaminejad, W. Gao, E. Wu, Z. A. Davies, H. Y. Y. Nyein, S. Challa, S. P. Ryan, H. M. Fahad, K. Chen, Z. Shahpar, S. Talebi, C. Milla, A. Javey, R. W. Davis, Autonomous sweat extraction and analysis applied to cystic fibrosis and glucose monitoring using a fully integrated wearable platform. *Proc. Natl. Acad. Sci. U.S.A.* **114**, 4625–4630 (2017).
19. A. J. Bandodkar, W. J. Jeang, R. Ghaffari, J. A. Rogers, Wearable sensors for biochemical sweat analysis. *Annu. Rev. Anal. Chem.* **12**, 1–22 (2019).

20. M. C. Brothers, M. DeBrosse, C. C. Grigsby, R. R. Naik, S. M. Hussain, J. Heikenfeld, S. S. Kim, Achievements and challenges for real-time sensing of analytes in sweat within wearable platforms. *Acc. Chem. Res.* **52**, 297–306 (2019).
21. W. He, C. Wang, H. Wang, M. Jian, W. Lu, X. Liang, X. Zhang, F. Yang, Y. Zhang, Integrated textile sensor patch for real-time and multiplex sweat analysis. *Sci. Adv.* **5**, eaax0649 (2019).
22. A. M. Zamarayeva, A. E. Ostfeld, M. Wang, J. K. Duey, I. Deckman, B. P. Lechêne, G. Davies, D. A. Steingart, A. C. Arias, Flexible and stretchable power sources for wearable electronics. *Sci. Adv.* **3**, e1602051 (2017).
23. J. Li, J. Zhao, J. A. Rogers, Materials and designs for power supply systems in skin-interfaced electronics. *Acc. Chem. Res.* **52**, 53–62 (2019).
24. A. J. Bandodkar, P. Gutruf, J. Choi, K. H. Lee, Y. Sekine, J. T. Reeder, W. J. Jeang, A. J. Aranyosi, S. P. Lee, J. B. Model, R. Ghaffari, C.-J. Su, J. P. Leshock, T. Ray, A. Verrillo, K. Thomas, V. Krishnamurthy, S. Han, J. Kim, S. Krishnan, T. Hang, J. A. Rogers, Battery-free, skin-interfaced microfluidic/electronic systems for simultaneous electrochemical, colorimetric, and volumetric analysis of sweat. *Sci. Adv.* **5**, eaav3294 (2019).
25. J. T. Reeder, J. Choi, Y. Xue, P. Gutruf, J. Hanson, M. Liu, T. Ray, A. J. Bandodkar, R. Avila, W. Xia, S. Krishnan, S. Xu, K. Barnes, M. Pahnke, R. Ghaffari, Y. Huang, J. A. Rogers, Waterproof, electronics-enabled, epidermal microfluidic devices for sweat collection, biomarker analysis, and thermography in aquatic settings. *Sci. Adv.* **5**, eaau6356 (2019).
26. J. Zhao, Y. Lin, J. Wu, H. Y. Y. Nyein, M. Bariya, L. C. Tai, M. Chao, W. Ji, G. Zhang, Z. Fan, A. Javey, A fully integrated and self-powered smartwatch for continuous sweat glucose monitoring. *ACS Sens.* **4**, 1925–1933 (2019).
27. S. Park, S. W. Heo, W. Lee, D. Inoue, Z. Jiang, K. Yu, H. Jinno, D. Hashizume, M. Sekino, T. Yokota, K. Fukuda, K. Tajima, T. Someya, Self-powered ultra-flexible electronics via nano-grating-patterned organic photovoltaics. *Nature* **561**, 516–521 (2018).
28. G. Chen, Y. Li, M. Bick, J. Chen, Smart textiles for electricity generation. *Chem. Rev.* **8**, 3668–3720 (2020).
29. A. J. Bandodkar, J.-M. You, N.-H. Kim, Y. Gu, R. Kumar, A. M. V. Mohan, J. Kurniawan, S. Imani, T. Nakagawa, B. Parish, M. Parthasarathy, P. P. Mercier, S. Xu, J. Wang, Soft, stretchable, high power density electronic skin-based biofuel cells for scavenging energy from human sweat. *Energy Environ. Sci.* **10**, 1581–1589 (2017).
30. F.-R. Fan, Z.-Q. Tian, Z. L. Wang, Flexible triboelectric generator. *Nano Energy* **1**, 328–334 (2012).
31. W. Seung, M. K. Gupta, K. Y. Lee, K.-S. Shin, J.-H. Lee, T. Y. Kim, S. Kim, J. Lin, J. H. Kim, S.-W. Kim, Nanopatterned textile-based wearable triboelectric nanogenerator. *ACS Nano* **9**, 3501–3509 (2015).
32. J. Chen, Y. Huang, N. Zhang, H. Zou, R. Liu, C. Tao, X. Fan, Z. L. Wang, Micro-cable structured textile for simultaneously harvesting solar and mechanical energy. *Nat. Energy* **1**, 16138 (2016).
33. J. Wang, S. Li, F. Yi, Y. Zi, J. Lin, X. Wang, Y. Xu, Z. L. Wang, Sustainably powering wearable electronics solely by biomechanical energy. *Nat. Commun.* **7**, 12744 (2016).
34. X. Pu, M. Liu, X. Chen, J. Sun, C. Du, Y. Zhang, J. Zhai, W. Hu, Z. L. Wang, Ultrastretchable, transparent triboelectric nanogenerator as electronic skin for biomechanical energy harvesting and tactile sensing. *Sci. Adv.* **3**, e1700015 (2017).
35. D. Liu, X. Yin, H. Guo, L. Zhou, X. Li, C. Zhang, J. Wang, Z. L. Wang, A constant current triboelectric nanogenerator arising from electrostatic breakdown. *Sci. Adv.* **5**, eaav6437 (2019).
36. Z. Liu, H. Li, B. Shi, Y. Fan, Z. L. Wang, Z. Li, Wearable and implantable triboelectric nanogenerators. *Adv. Funct. Mater.* **29**, 1808820 (2019).
37. S. S. Kwak, H.-J. Yoon, S.-W. Kim, Textile-based triboelectric nanogenerators for self-powered wearable electronics. *Adv. Funct. Mater.* **29**, 1804533 (2019).
38. X. Chen, Y. Song, Z. Su, H. Chen, X. Cheng, J. Zhang, M. Han, H. Zhang, Flexible fiber-based hybrid nanogenerator for biomechanical energy harvesting and physiological monitoring. *Nano Energy* **38**, 43–50 (2017).
39. Y. Song, H. Wang, X. Cheng, G. Li, X. Chen, H. Chen, L. Miao, H. Zhang, High-efficiency self-charging smart bracelet for portable electronics. *Nano Energy* **55**, 29–36 (2019).
40. C. J. de Ruiter, P. W. L. Verdijk, W. Werker, M. J. Zuidema, A. de Haan, Stride frequency in relation to oxygen consumption in experienced and novice runners. *Eur. J. Sport Sci.* **14**, 251–258 (2014).
41. K. Dong, Y.-C. Wang, J. Deng, Y. Dai, S. L. Zhang, H. Zou, B. Gu, B. Sun, Z. L. Wang, A highly stretchable and washable all-yarn-based self-charging knitting power textile composed of fiber triboelectric nanogenerators and supercapacitors. *ACS Nano* **11**, 9490–9499 (2017).
42. Z. Zhao, C. Yan, Z. Liu, X. Fu, L.-M. Peng, Y. Hu, Z. Zheng, Machine-washable textile triboelectric nanogenerators for effective human respiratory monitoring through loom weaving of metallic yarns. *Adv. Mater.* **28**, 10267–10274 (2016).
43. K. Dong, J. Deng, Y. Zi, Y.-C. Wang, C. Xu, H. Zou, W. Ding, Y. Dai, B. Gu, B. Sun, Z. L. Wang, 3D orthogonal woven triboelectric nanogenerator for effective biomechanical energy harvesting and as self-powered active motion sensors. *Adv. Mater.* **29**, 1702648 (2017).
44. W. Wang, A. Yu, X. Liu, Y. Liu, Y. Zhang, Y. Zhu, Y. Lei, M. Jia, J. Zhai, Z. L. Wang, Large-scale fabrication of robust textile triboelectric nanogenerators. *Nano Energy* **71**, 104605 (2020).
45. K. Chen, L. Zhang, X. Kuang, V. Li, M. Lei, G. Kang, Z. L. Wang, H. J. Qi, Dynamic photomask-assisted direct ink writing multimaterial for multilevel triboelectric nanogenerator. *Adv. Funct. Mater.* **29**, 1903568 (2019).
46. S. Wang, M. He, B. Weng, L. Gan, Y. Zhao, N. Li, Y. Xie, Stretchable and wearable triboelectric nanogenerator based on kinesio tape for self-powered human motion sensing. *Nanomaterials* **8**, 657 (2018).
47. Y.-C. Lai, J. Deng, S. Niu, W. Peng, C. Wu, R. Liu, Z. Wen, Z. L. Wang, Electric eel-skin-inspired mechanically durable and super-stretchable nanogenerator for deformable power source and fully autonomous conformable electronic-skin applications. *Adv. Mater.* **28**, 10024–10032 (2016).
48. Z. Wen, Y. Yang, N. Sun, G. Li, Y. Liu, C. Chen, J. Shi, L. Xie, H. Jiang, D. Bao, Q. Zhuo, X. Sun, A wrinkled PEDOT:PSS film based stretchable and transparent triboelectric nanogenerator for wearable energy harvesters and active motion sensors. *Adv. Funct. Mater.* **28**, 1803684 (2018).
49. J. Chen, H. Guo, X. Pu, X. Wang, Y. Xi, C. Hu, Traditional weaving craft for one-piece self-charging power textile for wearable electronics. *Nano Energy* **50**, 536–543 (2018).
50. S. Lu, L. Gao, X. Chen, D. Tong, W. Lei, P. Yuan, X. Mu, H. Yu, Simultaneous energy harvesting and signal sensing from a single triboelectric nanogenerator for intelligent self-powered wireless sensing systems. *Nano Energy* **75**, 104813 (2020).
51. Z. Zhou, X. Li, Y. Wu, H. Zhang, Z. Lin, K. Meng, Z. Lin, Q. He, C. Sun, J. Yang, Z. L. Wang, Wireless self-powered sensor networks driven by triboelectric nanogenerator for in-situ real time survey of environmental monitoring. *Nano Energy* **53**, 501–507 (2018).
52. K. Zhao, Z. L. Wang, Y. Yang, Self-powered wireless smart sensor node enabled by an ultrastable, highly efficient, and superhydrophobic-surface-based triboelectric nanogenerator. *ACS Nano* **10**, 9044–9052 (2016).
53. A. Ahmed, Z. Saadatnia, I. Hassan, Y. Zi, Y. Xi, X. He, J. Zu, Z. L. Wang, Self-powered wireless sensor node enabled by a duck-shaped triboelectric nanogenerator for harvesting water wave energy. *Adv. Energy Mater.* **7**, 1601705 (2017).
54. J. Wang, H. Zhang, Y. Xie, Z. Yan, Y. Yuan, L. Huang, X. Cui, M. Gao, Y. Su, W. Yang, Y. Lin, Smart network node based on hybrid nanogenerator for self-powered multifunctional sensing. *Nano Energy* **33**, 418–426 (2017).
55. Z. Lin, J. Chen, X. Li, Z. Zhou, K. Meng, W. Wei, J. Yang, Z. L. Wang, Triboelectric nanogenerator enabled body sensor network for self-powered human heart-rate monitoring. *ACS Nano* **11**, 8830–8837 (2017).
56. T. Zhao, C. Zheng, H. He, H. Guan, T. Zhong, L. Xing, X. Xue, A self-powered biosensing electronic-skin for real-time sweat Ca^{2+} detection and wireless data transmission. *Smart Mater. Struct.* **28**, 085015 (2019).

Acknowledgments

Funding: This work was supported by the California Institute of Technology Startup Grant and the Translational Research Institute through NASA NNX16AO69A. We gratefully acknowledge critical support and infrastructure provided for this work by the Kavli Nanoscience Institute at Caltech. **Author contributions:** W.G., Y.S., and H.Z. initiated the project. W.G. supervised the studies. Y.S. and J.M. led the experiments and collected the overall data. J.M., Y.S., and Y.Yu contributed to the system development, fabrication, and characterization. J.M. performed the electronic circuit design and test. Y.S. and H.W. contributed to FTENG preparation and characterization. Y.S. and Y.Yu contributed to sensor preparation and characterization. W.G., Y.S., J.M., and Y.Yang contributed to data analysis and cowrote the paper. All authors provided feedback on the manuscript. **Competing interests:** The authors declare that they have no competing interests. **Data and materials availability:** All data needed to evaluate the conclusions in the paper are present in the paper and/or the Supplementary Materials. Additional data related to this paper may be requested from the authors.

Submitted 25 April 2020

Accepted 14 August 2020

Published 30 September 2020

10.1126/sciadv.aay9842

Citation: Y. Song, J. Min, Y. Yu, H. Wang, Y. Yang, H. Zhang, W. Gao, Wireless battery-free wearable sweat sensor powered by human motion. *Sci. Adv.* **6**, eaay9842 (2020).

Science Advances

Wireless battery-free wearable sweat sensor powered by human motion

Yu Song, Jihong Min, You Yu, Haobin Wang, Yiran Yang, Haixia Zhang, and Wei Gao

Sci. Adv., **6** (40), eaay9842.
DOI: 10.1126/sciadv.aay9842

View the article online

<https://www.science.org/doi/10.1126/sciadv.aay9842>

Permissions

<https://www.science.org/help/reprints-and-permissions>